Analysis of Flow Patterns in Structured Zickzack-Packings for Rotating Packed Beds using Gamma-Ray Computed Tomography

Loll, R.; Nordhausen, L.; Bieberle, A.; Schubert, M.; Pyka, T.; Koop, J.; Held, C.; Schembecker, G.;

Originally published:

September 2023

Industrial & Engineering Chemistry Research 62(2023), 15625-15634

DOI: https://doi.org/10.1021/acs.iecr.3c02252

Analysis of Flow Patterns in Structured Zickzack-Packings for Rotating Packed Beds using Gamma-Ray Computed Tomography

Rouven Loll[1,2], Lisa Nordhausen[1], André Bieberle[3], Markus Schubert[3,4], Tobias Pyka[1,2], Jörg Koop[2], Christoph Held[1,], Gerhard Schembecker[2]*

1: TU Dortmund University, Department of Biochemical and Chemical Engineering, Laboratory of Fluid Separations, Emil-Figge-Straße 70, 44227 Dortmund, Germany

2: TU Dortmund University, Department of Biochemical and Chemical Engineering, Laboratory of Plant and Process Design, Emil-Figge-Straße 70, 44227 Dortmund, Germany

3: Helmholtz-Zentrum Dresden-Rossendorf, Institute of Fluid Dynamics, Bautzener Landstraße 400, 01328 Dresden

4: Technische Universität Dresden, Chair of Chemical Process Engineering, 01069 Dresden

*Corresponding author: christoph.held@tu-dortmund.de

KEYWORDS: Rotating packed beds, HIGEE, packing design, 3D printing, deaeration, fluid dynamics, pressure drop, mass transfer

ABSTRACT

Rotating Packed Beds (RPBs) are increasingly used in academia and industry for separation processes, but a lack of knowledge about fluid dynamics and liquid maldistribution still limits understanding the mass transfer inside. Recently, structured Zickzack packings (ZZ packings) were designed that promise to provide homogeneous liquid distribution throughout the packing volume. In this study, the fluid dynamics of a water-air system in ZZ packings were characterized at atmospheric pressure and 20°C. For decreasing rotational speeds, a strongly increasing wet pressure drop was observed below 500 rpm due to a formation of a liquid wreath in front of the inner packing edge, and flooding of the rotor eye was visually detected at rotational speeds lower than 300 rpm. At rotational speeds greater than the flooding limit, the fluid dynamics of a single ZZ packing were found to be equal to a stacked two-level ZZ packing. In addition, gamma-ray computed tomography (CT) was used to non-invasively study the liquid distribution inside the rotating packing at multiple scanning planes along the packing height for selected operating conditions. The scans revealed that liquid maldistribution occurred at rotational speeds lower than 1200 rpm, while the liquid was perfectly distributed throughout the packing volume at rotational speeds greater than 1200 rpm.

ABSTRACT GRAPHIC

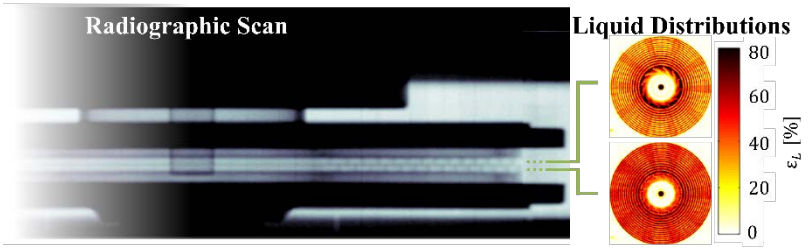

1. Introduction

Rotating packed beds (RPBs) are an efficient means towards process intensification, and RPBs were first introduced by Ramshaw and Mallinson in 1981[1]. Since then, RPBs have gained attention in research, and an increasing number of industrial applications in distillation, absorption, or desorption is reported[2–4]. Phase contacting and mass transfer in the RPB packing are intensified through the rotation of the packed bed, ultimately enabling a reduction of the equipment size compared to conventional columns[3,5]. This is advantageous for prefabrication and transport of the equipment from manufacturers to customers[6], for retrofitting of existing plants[3,4,6] and for installations in space-limited environments like off-shore applications[3,4,7,8]. As a result of short fluid residence times and the accordingly short response time, the RPB technology is promising for applications that require high operation flexibility[6].

However, the technical maturity of RPBs is still low compared to conventional gravity-driven columns[2,3,9]. A better knowledge about the fluid dynamics in RPBs is required to understand the mass transfer behavior and to derive scale-up rules[2,9,10]. Previous studies[11] revealed severe liquid maldistribution along the radius and circumference of porous packings such as isotropic metal-foam packings conventionally used in RPBs. Thus, new packing designs are required to achieve efficient contacting of the fluid phases throughout the entire volume of an RPB packing[3,12]. In the recent years, 3D printing technologies have emerged as a promising tool supporting the development of new packing designs[13]. In addition to anisotropic[14] and multi-liquid-inlet[15] wire-mesh packings, various special structured packings[16,17] were suggested to homogenize the liquid distribution.

The so-called Zickzack packing (ZZ packing) belongs to these specially designed structured packings, and the ZZ packing has shown to outperform isotropic porous metal-foam packings and wire meshes in distillation[16] and deaeration[18] experiments. Similar to the structure of the widely

used rotating zigzag beds (RZBs), the ZZ packing consists mainly of overlapping concentric baffles, where the upper and the lower baffles rotate at the same speed. The tray-like baffle design of the ZZ packing guides the fluid phases through the packing on a zigzag path of approximately constant cross-sectional area, with the aim of distributing the liquid holdup on the baffles (without perforation) uniformly throughout the packing. One open question is how to increase the capacity of RPBs equipped with ZZ packings. One option is to reduce the number of baffles per packing volume for an increased total throughput. However, this reduces the total liquid holdup and also the liquid droplet formation, both of which is disadvantageous for mass transfer. The other possibility is to design a multi-level ZZ packing, which allows increasing cross-sectional area in order to keep the fluid loads.

A variety of methods have been used in different studies to measure holdup distributions and flow patterns in RPB packings and to detect liquid maldistribution[19,20]. Early studies used cameras to optically evaluate liquid flows inside the rotor[21] or conductivity measurements to detect liquid holdup distributions in the rotor[22,23]. More recent studies have used radiation-based computed tomography (CT) as a non-invasive tool to investigate in more detail the flow patterns and the liquid holdup distributions inside the packings of RPBs[11,24–26]. The radiation-based CT measurement technique allows detecting the liquid-phase distribution throughout the entire volume of the packing structure. It was successfully synchronized with the rotation of the packing[11] without disturbing the two-phase flow by any sensors[24]. In addition, optically transparent equipment is not required[11]. In the past, X-ray CT has been used by Yang et al.[24] and Liu et al.[25] to detect phase distributions in small-scale RPBs with packing diameters of up to 82 mm. Groß et al.[11] and Gładyszewski et al.[26] used high-energy gamma-ray CT to investigate a pilot-scale RPB equipped with metal-foam packings with up to 450 mm outer diameter.

In this study, the fluid dynamics in ZZ packings were first characterized using standard wet pressure drop measurements for a wide range of gas and liquid flow rates and rotational speeds. Additionally, flooding conditions in the rotor eye at low rotational speeds were characterized using a sight glass. A stacked version of the ZZ packing was developed to study the fluid dynamics and mass transfer upon scaling-up of the ZZ packing, keeping the fluid loads constant by adjusting the cross-sectional area for the fluid flow through the stacking process. Finally, gamma-ray CT measurements were performed for selected operating conditions of the RPB. This allowed analyzing the liquid distribution inside the ZZ packing at the very center of the baffle height of the lower and upper baffle layer.

2. Materials and Methods

2.1 Structure and Principles of the ZZ packing for RPBs.

The basic internal configuration of an RPB equipped with a ZZ packing is schematically shown in Figure 1. It details the gamma-ray CT scanning planes applied in this work and the liquid and gas flow paths that occur inside the packing.

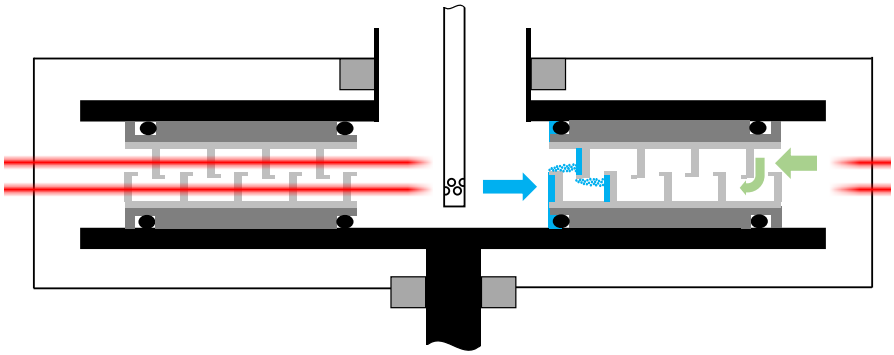

Figure 1. Left: scanning planes at which gamma-ray CT is performed in this work (red). Right: basic fluid flow patterns of a gas flow (green) and a liquid flow (blue) through a rotating Zickzack packing structure (gray).

A more detailed description of the baffle arrangement in the packing, including the geometric specifications of the structure, is given in Figure 2.

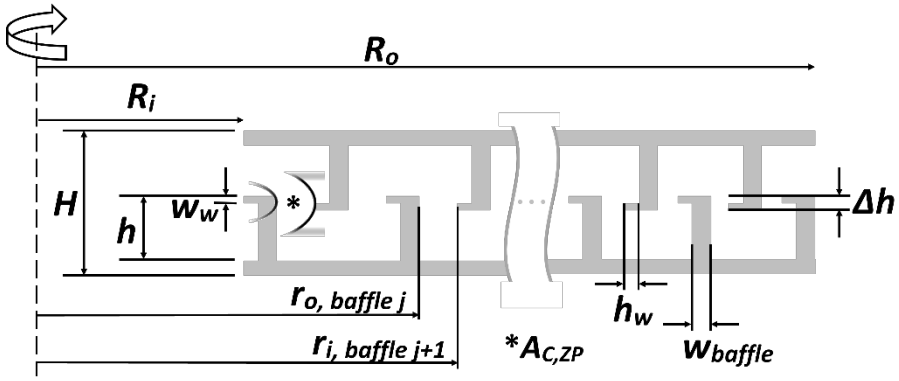

Figure 2. Cross-section of the investigated Zickzack packing with packing height (H), baffle height (h), axial overlap of baffles (Δh), weir height (h_w), weir width (w_w), baffle width (w_{baffle}), cross-sectional area ($A_{c,ZP}$), inner radius (R_i) and outer radius (R_o) of the packing as well as inner radius (r_i) of baffle j+1 and outer radius (r_o) of baffle j.

The ZZ packing was designed according to an equal-area principle. The baffles were positioned in the packing so that the annular cross-sectional area for the fluid flow between each pair of baffles ($A_{c,ZP}$, cf. Figure 2) is constant over the radius of the packing (cf. eq 1).

$$A_{c,ZP} = \pi \left(r^2_{i,baffle\,j+1} - r^2_{o,baffle\,j} \right) = const. \quad (1)$$

The gas load, commonly described by the gas capacity factor F_G, is calculated according to eq 2 and the specific liquid load LL is calculated as given in eq 3.

$$F_G = \frac{\dot{V}_G}{A_{c,ZP}} \sqrt{\rho_G} \quad (2)$$

$$LL = \frac{\dot{V}_L}{A_{c,ZP}} \quad (3)$$

$\dot{V}_G$ is the volumetric gas flow rate, $\dot{V}_L$ the volumetric liquid flow rate and ρ_G the density of the gas phase. Both, F_G and LL are approximately constant over the radius of the ZZ packing, whereas for isotropic porous packings, such as metal foams or knitted meshes, F_G and LL decrease with increasing radius. F_G and LL in these packing types are thus often specified at the innermost radius of the packing with the smallest cross-sectional area, which, accordingly, results in the highest loads.

2.2 Used ZZ packing and RPB Specifications.

The dimensions and properties of the unstacked ZZ packing used for the fluid dynamic investigations are summarized in table 1. The packing was composed of ten identical segments, printed from Formlabs Hi-temp resin in a Formlabs Form 2 3D printer, and the segments were bonded with two-component epoxy adhesive Technicoll 9464 (cf. Figure 3A). For mechanical stability, the ZZ structure was supported by 10 radial rods and 145 horizontal rods with 0.5 mm diameter in each packing segment (cf. Figure 3). To prevent gas and liquid bypasses between the packing and the upper and lower rotor plates, O-ring seals (made of ethylene propylene diene monomer rubber) with a diameter of 3.53 mm were put between packing and rotor plates.

Table 1. Dimensions and properties of the unstacked ZZ packing.

Packing attribute	specification
Inner packing radius R_i \ mm	73.0
Outer packing radius R_o \ mm	190.0
Height of the packing structure H \ mm	10.0
Free cross-sectional area $A_{c,ZP}$ \ mm²	1400
Baffle height h \ mm	4.5

Radial baffle width w_{baffle} \ mm	1.3
Weir height h_w \ mm	1.0
Weir width w_w \ mm	0.5
Axial overlap of baffles Δh \ mm	2 w_w
Number of baffles in the upper layer	14
Number of baffles in the lower layer	15

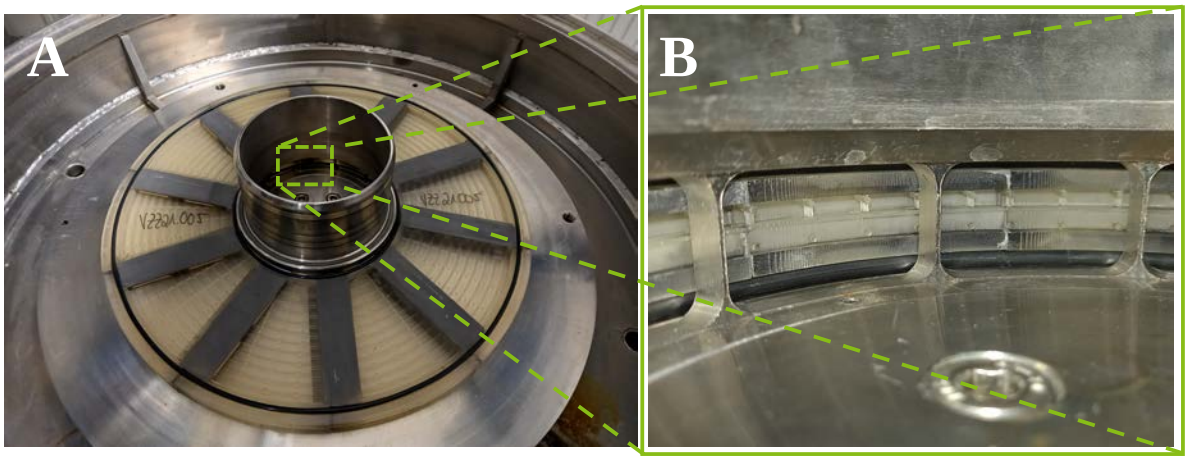

Figure 3. A: Unstacked Zickzack packing made of bonded ten identical segments, including O-ring seals at the top and at the bottom of the packing to prevent bypass flows, centered around the inner packing support ring on the lower rotor plate. B: zoom inside the rotor eye showing the axial struts of the inner packing support ring in front of the unstacked sealed Zickzack packing in the middle of the photograph.

The RPB used in this study was purchased from Omnikon and has an outer rotor radius of 250 mm and an inner casing radius of 325 mm. Packings inside this RPB can have a maximum height of 25 mm. The RPB is sealed by a three-ring graphite floating ring seal by EagleBurgmann.

The scale-up methodology by stacking the ZZ packing was investigated using slightly modified ZZ packings: a single-level ZZ packing and a two-level ZZ packing. In order to make the two-level ZZ packing fit into the RPB used, the height of the sealing structure[18] on top and on the

bottom of these ZZ packings was reduced from 5.0 mm to 2.5 mm compared to the previously investigated unstacked ZZ packing. The reduced height of the seal structure required the use of O-rings with 2.62 mm diameter instead of 3.53 mm. Further, the innermost baffle of the original unstacked ZZ packing design (cf. Figure 1) was omitted in these two packings to prevent the liquid in the innermost baffle of the upper level from overflowing into the lower level of the two-level ZZ packing. Thus, mass transfer between the levels of the two-level ZZ packing was impossible. Liquid distribution was assured by a 48-point nozzle for the unstacked and single-level ZZ packing, and a 2x48-point nozzle for the two-level ZZ packing. It was gravimetrically verified that the liquid volume for the upper level of the ZZ packing differs by less than 9 % from the lower level.

2.3 Deaeration experiments

The deaeration experiments in the RPB were performed by stripping oxygen from tap water using nitrogen (purity > 99.999%, by Messer) in countercurrent flow at atmospheric pressure and 20°C. Prior to the experiments, the tap water had been aerated with compressed air. In addition, the airtightness of the machine was verified by first flushing the plant with nitrogen and then applying a small vacuum in the RPB through the rotor while checking whether oxygen from the laboratory atmosphere leaks into the plant. Further details about the experimental setup can be found in a previous study[18]. To quantify the separation efficiency in the RPB in counter-current operation, the Kremser equation[27] was used for determining the number of theoretical equilibrium stages n_{th}. By balancing the molar flow rates of gas and liquid in the process and assuming constant pressure, constant molar flow rates ($\dot{n}_L$, $\dot{n}_G$) and validity of Henry´s law, n_{th} was calculated using eq 4[27]

$$n_{th} = \frac{ln\left(\frac{x_{in} - \frac{y_{in}\,p}{K^{px}_{O_2,H_2O}}}{x_{out} - \frac{y_{in}\,p}{K^{px}_{O_2,H_2O}}}\left(1 - \frac{\dot{n}_L\,p}{\dot{n}_G\,K^{px}_{O_2,H_2O}}\right) + \frac{\dot{n}_L\,p}{\dot{n}_G\,K^{px}_{O_2,H_2O}}\right)}{ln\left(\frac{\dot{n}_G\,K^{px}_{O_2,H_2O}}{\dot{n}_L\,p}\right)} \quad (4)$$

with the molar fractions of oxygen at liquid inlet x_{in} and outlet x_{out}, and at the gas inlet y_{in}, the pressure p, the Henry coefficient $K^{px}_{O_2,H_2O}$, the molar liquid and gas flow rates $\dot{n}_L$ and $\dot{n}_G$.

2.4 Gamma-Ray Computed Tomography

To quantify the local liquid fraction at each position of the rotor within a scanning plane, the radiation attenuation at each position is determined using a gamma-ray CT scanner. This device essentially consists of a collimated Cs^{137} isotopic source and an oppositely positioned radiation detector arc containing 320 individual detectors positioned with their focus towards the isotopic source[28]. Typically, a CT scanner is rotating around the object of investigation[29]. However, the CT scanner was fixed in our experiments, and its projection data stream was synchronized with the rotational speed of the packing f_{rot}, the so-called time-averaged angular-resolved CT scanning method[11,30]. This setup was chosen since our study aimed at analyzing the liquid distribution inside rotating ZZ packings, while packing structures were clearly visible. As the CT scanner provides a detector sampling frequency of f_{samp} = 22 kHz, sufficient projection data are acquired even at the highest rotational speed of 1800 rpm, i.e. N_{proj} = 22 kHz / 30 Hz = 733 projections. Thus, a suitable scanning time, i.e. projection averaging time, was determined in order to provide correct statistics. In order to synchronize the data stream with the packing rotation, a zero-crossing signal was taken from the RPB using a fast response HALL sensor aimed at the rotor drive shaft[11]. The rotational speed between consecutive zero crossings was assumed to be constant.

To extract quantitative local liquid fractions from the reconstructed attenuation coefficients distribution $\mu_{\mathrm{op}}(i,k)$ during operation at pixel position i and k within the scanning plane, an additional reference scan of the dry attenuation coefficients distribution $\mu_{\mathrm{dry}}(i,k)$ without liquid in the packing was required. Finally, the liquid reference value $\bar{\mu}_{\mathrm{liq}}$ was extracted from the liquid distributor pipe area in $\mu_{\mathrm{op}}(i,k)$. Thus, the liquid fraction distribution (cf. eq 5) was calculated.

$$\varepsilon_L(i,k) = \frac{\mu_{\mathrm{dry}}(i,k) - \mu_{\mathrm{op}}(i,k)}{\mu_{\mathrm{dry}}(i,k) - \bar{\mu}_{\mathrm{liq}}} \qquad (5)$$

Finally, the angular-averaged radial liquid fraction profile (cf. eq 6) was obtained, allowing evaluation of the liquid fraction distributions along the radial cross-section of the ZZ packing.

$$\varepsilon_{L,aa}(r) = \sum_{\varphi=0°}^{360°} \mathrm{cart2pol}(\,\varepsilon(i,k)\,) \qquad (6)$$

3. Results and discussion

3.1 Pressure drop in unstacked ZZ packings

The total wet pressure drop Δp in the RPB equipped with the unstacked ZZ packing is shown in Figure 4. As previously observed by Loll et al.[18], a pressure drop minimum can be observed, and the value of the minimum as well as the n_{rot} at which this minimum occurs depend on the fluid rates. At a gas flow rate of $\dot{V}_{G,1}$ = 0.5 m^3 h^{-1} and a liquid flow rate of $\dot{V}_{L,1}$ = 0.48 m^3 h^{-1}, Δp increased monotonically with n_{rot} for n_{rot} > 500 rpm. Upon doubling the fluid loads ($\dot{V}_{G,3}$, $\dot{V}_{L,3}$), the described pressure drop minimum was detected at 1200 rpm. Upon tripling the rates to $\dot{V}_{G,5}$ = 1.5 m^3 h^{-1} and $\dot{V}_{L,5}$ = 1.44 m^3 h^{-1}, Δp decreased with increasing n_{rot} and a minimum could not be observed in the n_{rot} ranges measured.

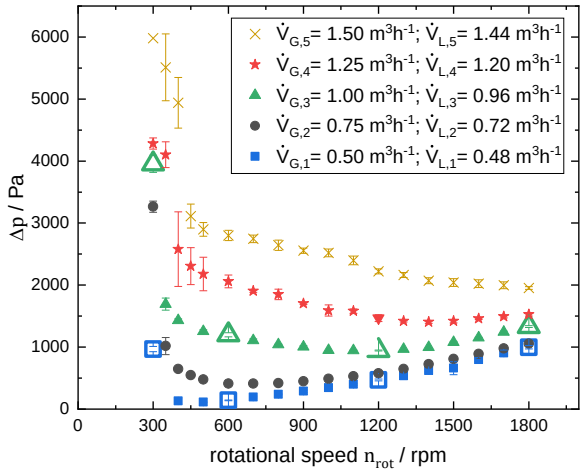

Figure 4. Total wet pressure drop Δp in the RPB equipped with the unstacked ZZ packing at different rotational speeds n_{rot} at different fluid flow rates of tap water and air at 20°C and atmospheric pressure. Squares: $\dot{V}_{G,1}$ = 0.5 m^3 h^{-1} and $\dot{V}_{L,1}$ = 0.48 m^3 h^{-1}, points: $\dot{V}_{G,2}$ = 0.75 m^3 h^{-1} and $\dot{V}_{L,2}$ = 0.72 m^3 h^{-1}, triangles: $\dot{V}_{G,3}$ = 1 m^3 h^{-1} and $\dot{V}_{L,3}$ = 0.96 m^3 h^{-1}, stars: $\dot{V}_{G,4}$ = 1.25 m^3 h^{-1} and $\dot{V}_{L,4}$ = 1.20 m^3 h^{-1} and crosses: $\dot{V}_{G,5}$ = 1.5 m^3 h^{-1} and $\dot{V}_{L,5}$ = 1.44 m^3 h^{-1}. Data are given in Table S1 in the Supporting Information.

Δp mainly consists of the centrifugal head and the frictional pressure drop of the packing next to smaller contributions by gas flows in the RPB eye and casing[6,31]. In general, a decrease in Δp with decreasing n_{rot} can be explained by a decreasing centrifugal head generated by the rotor[5,31,32]. However, if the frictional pressure drop increases at a higher rate, lower than a certain rotational speed, due to increasing liquid holdup in the rotor, Δp will increase upon further reducing n_{rot} [16,18]. Thus, the pressure drop minimum is attributed to a balance of both effects described. Furthermore, an increase in the rotational speed at which the pressure drop minimum occurs with increasing fluid loads has also been attributed to an increasing liquid holdup in ZZ packings[18].

In contrast, Δp increased sharply with decreasing n_{rot} < 500 rpm for all fluid loads studied according to the results shown in Figure 4. A pulsating liquid ring interspersed with the gas phase formed in the rotor eye in front of the packing, which also is illustrated in Figure 5. This will henceforth be referred to as a liquid wreath, as previously termed by Li et al.[31] for a similar observation in the eye of a partially disassembled RZB without its gas outlet. At low rpms, the amount of liquid in the rotor increases causing pulsation of the wreath.

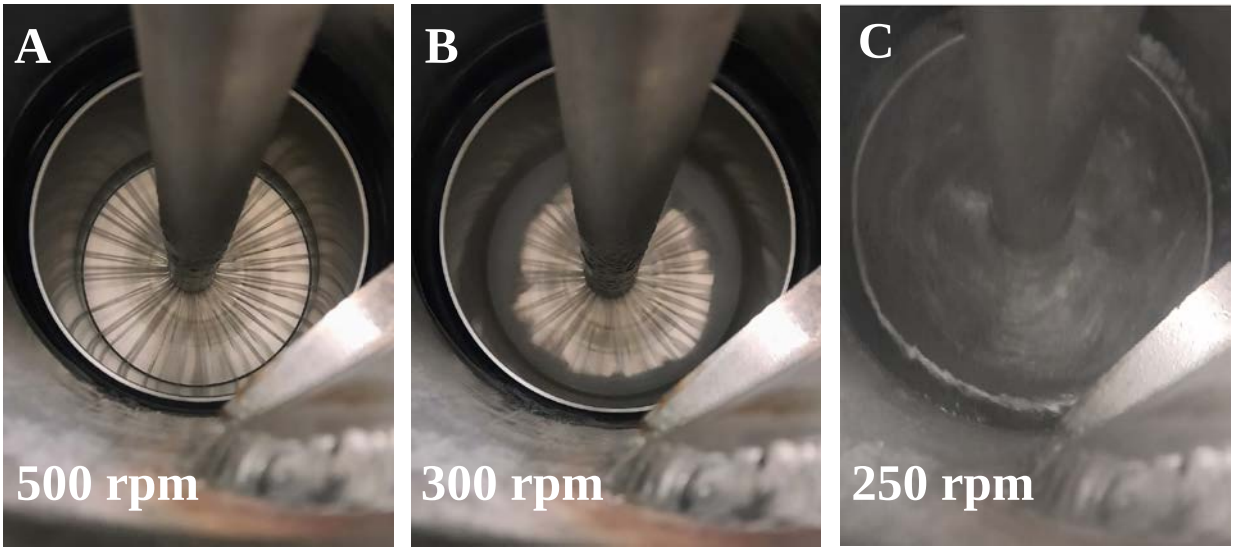

Figure 5. Fluid-dynamic regimes observed in the rotor eye for measurements with an air flow rate of $\dot{V}_{G,3}$ = 1 m^3 h^{-1} and a tap water flow rate of $\dot{V}_{L,3}$ = 0.96 m^3 h^{-1} at 20°C and atmospheric pressure in the unstacked ZZ packing. A: Liquid jets from the liquid distributor pipe to the packing at 500 rpm; B: Liquid jets impinge on a liquid wreath in front of the packing at 300 rpm; C: The rotor eye fills up with liquid, through which gas bubbles erupt.

Figure 5A illustrates the liquid jets into the ZZ packing at n_{rot} = 500 rpm, which is representative also for all measurements at n_{rot} > 500 rpm. However, at 300 rpm, a pulsating liquid wreath was visible in the rotor eye in front of the packing (Figure 5B). The formation of this liquid wreath can be explained by a decreased centrifugal acceleration driving the liquid flow into

the packing against the countercurrently flowing gas. This explains the observed (cf. Figure 4) distinctly increasing Δp upon reducing n_{rot} to values < 500 rpm. Further reducing n_{rot} to values < 300 rpm destroyed the liquid wreath, while liquid continuously accumulated in the rotor eye (cf. Figure 5C). Hence, a significant fraction of the liquid phase leaves the RPB through the gas outlet pipe (bottom right-hand corner of the sub-figures in Figure 5) without having passed through the rotor at all. As this regime is not desired during RPB operation, it is not investigated further in this work. It should be noted, that the n_{rot} at which liquid-wreath formation and flooding occur depends on the (inner) packing diameter due to the different centrifugal forces acting on the liquid phase. Thus, the quantitative results of this work are not transferable to different packing dimensions.

3.2 Stacked ZZ packings

The total wet pressure drop Δp and the number of theoretical stages n_{th} for the desorption of oxygen from aerated tap water with nitrogen are shown in Figure 6. The results were obtained in the RPB equipped with the single-level ZZ packing and compared with the two-level ZZ packing.

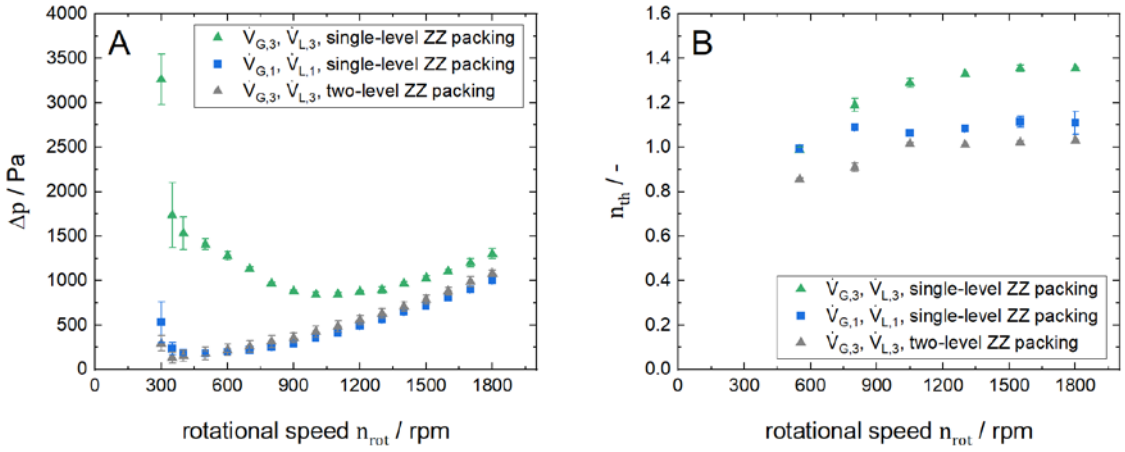

Figure 6. Total wet pressure drop Δp (A) and number of theoretical stages n_{th} (B) at different rotational speeds n_{rot}, at 20°C and atmospheric pressure at fluid flow rates of squares: $\dot{V}_{G,1}$ = 0.5 m^3 h^{-1} nitrogen, $\dot{V}_{L,1}$ = 0.48 m^3 h^{-1} aerated tap water in the RPB equipped with a single-level ZZ packing and at fluid flow rates of triangles: $\dot{V}_{G,3}$ = 1.0 m^3 h^{-1} nitrogen, $\dot{V}_{L,3}$ = 0.96 m^3 h^{-1} aerated tap water in the RPB equipped with a green: single-level ZZ packing and grey: two-level ZZ packing. The data are given in Table S2 and S3 in the Supporting Information.

The measurements with the single-level ZZ packing at $\dot{V}_{G,1}$ and $\dot{V}_{L,1}$ are used as a benchmark and show Δp and n_{th} values, which are consistent with previous measurements[18]. Compared to this benchmark, the pressure drop curve was nearly identical upon using the two-level ZZ packing at doubled volume flow rates ($\dot{V}_{G,3}$ and $\dot{V}_{L,3}$). This indicates that the fluid dynamics in both levels of the ZZ packing are equal. n_{th} was only slightly lower compared to the benchmark, which can be explained by the small difference in liquid flow rate in the two levels and by the fact that the casing of the RPB was not scaled to the fluid flow rates in this case. This demonstrates that the fluid dynamic conditions inside the single-level ZZ packing are maintained in stacked packings for correspondingly higher throughputs.

The effect of doubling the fluid flow rates in the single-level ZZ packing is also illustrated in Figure 6. At 550 rpm and upon doubling the fluid flow rates, n_{th} remained the same while Δp increased by a factor of 6. At higher n_{rot}, n_{th} was significantly higher at the increased fluid loads while the difference in Δp decreased to 30% compared to the benchmark system. This can partly be explained by increased liquid holdup but also by higher turbulence and a better dispersion of the liquid phase at higher fluid loads. Therefore, higher pressure drop can be compensated by higher separation efficiency upon increasing the throughput in a single-level ZZ packing compared to a multi-level ZZ packing. However, it is likely that the two-level ZZ packing can process a higher maximum throughput than the single-level ZZ packing.

3.3 Holdup measurements in unstacked ZZ packings

The unstacked ZZ packing was investigated in detail with gamma-ray CT. Since the ZZ packing has a diameter of 380 mm and the height of the packing is only slightly greater than the height of the gamma-ray detector (approximately 4 mm), a great deal of effort was put into the correct alignment of the scanning plane positions and the packing. In order to achieve optimum planarity between the scanning planes and the center of the baffle height of both layers, radiographic scans were iteratively performed at 0° and 90° RPB angular positions with a height discretization of 1 mm until the sharpness of the upper and lower rotor plates was best matched at both angular positions. The final alignment between the gamma-ray CT scanner and the RPB is shown in Figure 7A. A scanning time of 15 minutes was selected. For image reconstruction, the SIRT algorithm[33] was selected and applied to a grid with a pixel size of 1 mm by 1 mm.

In order to selectively identify the liquid holdup distribution inside the rotor, it was first necessary to determine the exact positions of packing material and metal parts, as well as the free volume for liquids as a reference. The results of these reference measurements are shown in

Figure 7B and Figure 7C for 1800 rpm. Figure 7D shows the alternating arrangement of the upper and lower baffles of the ZZ structure.

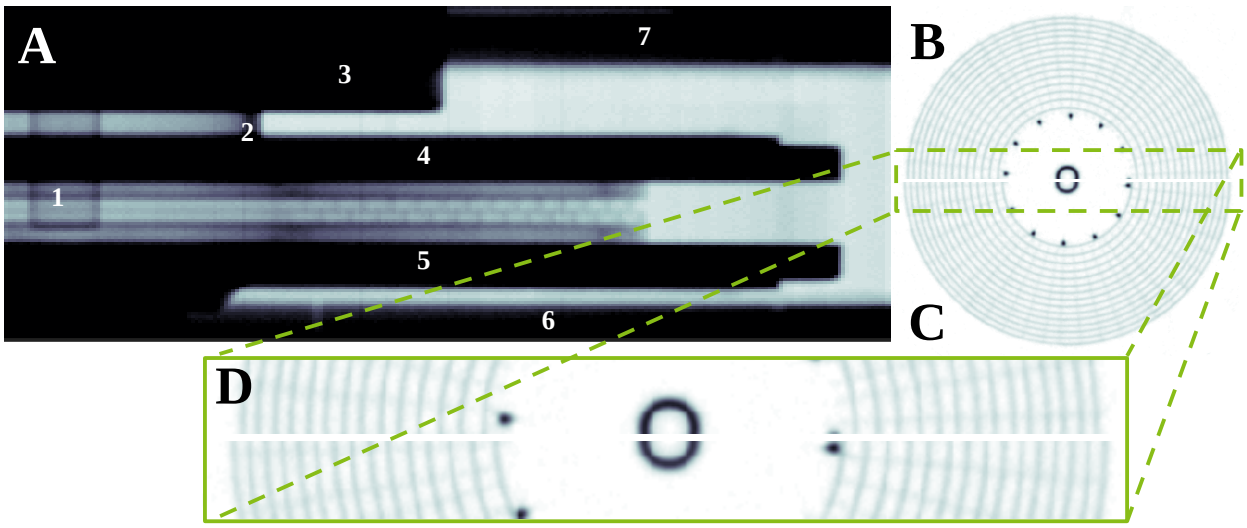

Figure 7. A: Radiographic scan of the rotating dry RPB internals showing liquid distributor pipe (1), inner packing support ring (2), seal housing for the three floating ring seals (3), upper (4) and lower (5) rotor plates with the unstacked Zickzack packing in between, RPB casing (6) and lid (7); B+C: CT scans at 1800 rpm showing the distribution of the packing material and the steel parts of the rotor, given for half of the packing in the upper (B) and lower baffle layers (C); D: Close up of the upper and lower baffles.

Each angular baffle is clearly visible in Figure 7, nicely showing also that the radial distance between adjacent baffles decreases with increasing radius due to the equal-area principle guiding the design of the ZZ structure. The radial rods supporting the baffles are also visualized and it can be seen that the innermost baffle in the lower layer of baffles is in contact with the inner packing support ring (cf. Figure 3B). Further, the empty liquid distributor pipe in the center of the RPB is visible. The angular-averaged radial profiles of the liquid fraction as well as the liquid fraction distributions in the ZZ packing as a function of n_{rot} for $\dot{V}_{G,3}$ and $\dot{V}_{L,3}$ are illustrated in Figure 8.

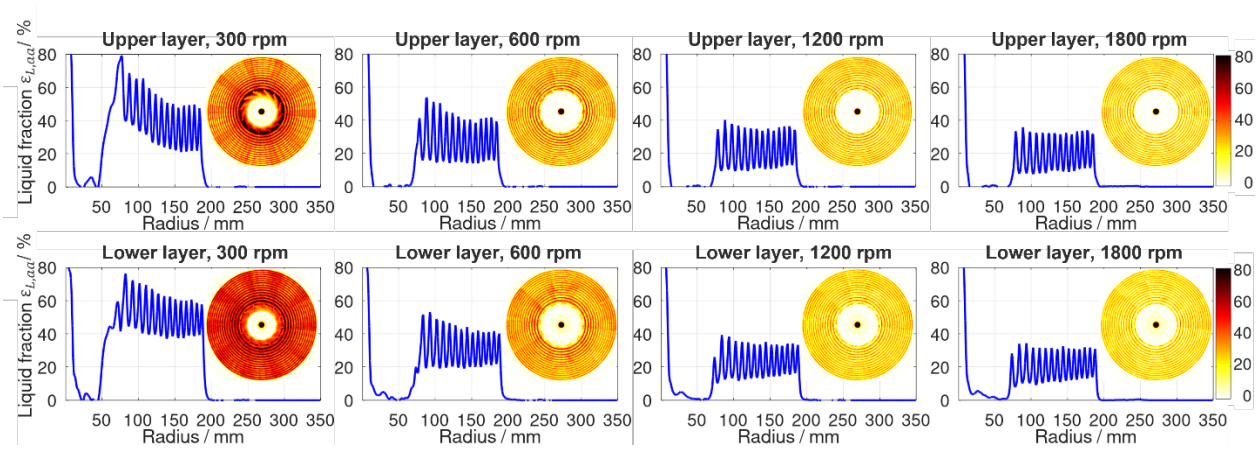

Figure 8. Effect of the rotational speed n_{rot} on the angular-averaged radial profiles of the liquid fraction $\varepsilon_{L,aa}$ and on the liquid fraction distributions in the upper and lower baffle layers of the unstacked ZZ packing at 300 to 1800 rpm and constant fluid flow rates of air: $\dot{V}_{G,3}$ = 1 m^3 h^{-1} and tap water: $\dot{V}_{L,3}$ = 0.96 m^3 h^{-1}, at 20°C and atmospheric pressure. The liquid fraction distribution is illustrated as an enlarged sketch in the Supporting Information in Figure S1.

The liquid holdup on the baffles is shown in the radial profiles of Figure 8 as 14 peaks in the upper layer and 15 peaks in the lower layer. These peaks of the saw curves are located directly in front of the baffles as intended by the design of the ZZ packing structure (cf. Figure 1). This is exemplarily illustrated also in the Supporting Information in Figure S2 for the upper baffle layer at 300 rpm. The minima points in these saw curves represent the liquid flow between the baffles. Peaks of equal height indicate a homogeneous liquid distribution in the baffles over the radius of the packing at higher n_{rot}. The increasing values of the low points with increasing radius can be explained by an overlapping of the peak tails of the converging peaks. An increasingly uneven liquid distribution over the radius was present upon decreasing n_{rot}, as higher peaks showed a higher liquid fraction on the inner baffles compared to the baffles at the outer radii. As n_{rot} was reduced to about 300 rpm (at which the liquid wreath appeared in front of the packing), the liquid

fraction between the adjacent baffles at the inner radii also increased. Furthermore, the difference between the liquid fractions at upper and lower baffles increases with decreasing n_{rot} for all radii. This indicates that the influence of the gravitational acceleration on the liquid flow path and the shape of the liquid body on the baffles is only negligible at $n_{rot} \geq 1200$ rpm for the rotor dimensions given. In the liquid distribution images, the liquid inside the wreath at 300 rpm and the areas of gas flow through the wreath can be identified and compared with the visual inspection (cf. Figure 8 and Figure 5B). The gamma-ray CT scans show that the gas phase passes along the struts of the inner packing support ring in a vortex-like shape directed towards the center of the rotor eye with the filled liquid distributor pipe. To a lesser extent, this gas/liquid segregation was also present at the first upper and lower baffles at higher n_{rot}. The same observations were made in additional measurements with a larger ZZ packing (1.2 times the outer diameter, cf. Figure S3). Figure 9 summarizes the evolution of the liquid fraction distribution in radial and axial directions for $\dot{V}_{G,3}$ and $\dot{V}_{L,3}$ as well as for the lower fluid flow rates $\dot{V}_{G,1}$ and $\dot{V}_{L,1}$.

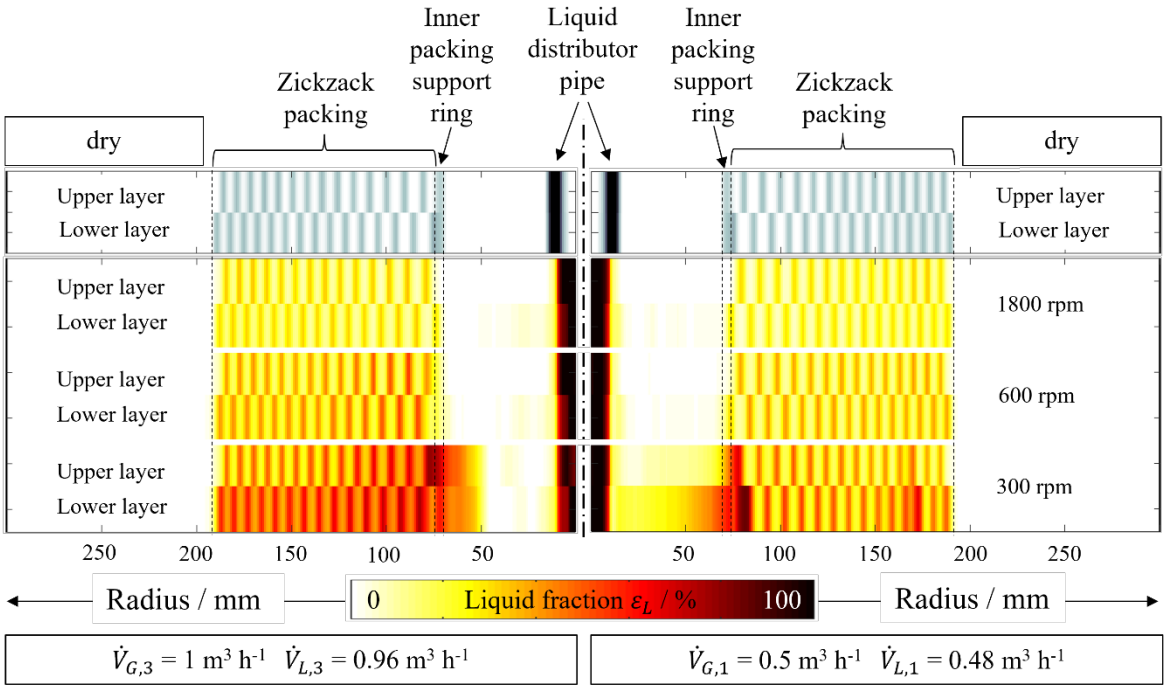

Figure 9. Summary of axial and radial distributions of the dry rotor elements and the corresponding liquid fractions in the unstacked ZZ packing at rotational speed n_{rot} of 300 to 1800 rpm and fluid flow rates of air and tap water of $\dot{V}_{G,1}$ = 0.5 m^3 h^{-1}, $\dot{V}_{L,1}$ = 0.48 m^3 h^{-1} and $\dot{V}_{G,3}$ = 1 m^3 h^{-1}, $\dot{V}_{L,3}$ = 0.96 m^3 h^{-1}, at 20°C and atmospheric pressure, averaged over twelve 30° segments for the upper and lower baffle layers.

At the lowest fluid loads studied ($\dot{V}_{G,1}$ and $\dot{V}_{L,1}$), the segregation of gas and liquid in the wreath in front of the packing was present rather in axial direction as the wreath expands less into the upper scanning plane with the upper layer of baffles (the angular-averaged radial profiles of the liquid fraction and the liquid fraction distributions can be found in the Supporting Information in Figure S4). At 300 rpm, the flow phenomena in the packing also resulted in an increased liquid fraction at baffles 11 and 12 in the upper layer and at baffles 12 and 13 in the lower layer. However, the radial maldistribution was already negligible at 600 rpm for these lower fluid loads. As with the higher fluid loads, at $n_{rot} \geq$ 1200 rpm, the influence of the gravitational acceleration on the liquid flow path and the surface of the liquid body on the baffles is negligible.

The liquid fraction distributions at $\dot{V}_{G,3}$, $\dot{V}_{L,3}$(cf. Figure 8) and $\dot{V}_{G,1}$, $\dot{V}_{L,1}$(cf. Figure S4) do not reveal any dry spots in the packing, demonstrating the liquid distribution capability of the baffle design. Slightly uneven liquid distribution in the circumferential direction was present only at lower n_{rot}. The circumferential slip velocity between liquid and packing material increased with decreasing n_{rot}, resulting in locally increased liquid fraction in front of flow obstacles (support rods and glued edges of the individual packing segments) (cf. Figure 3A). This is not the case at $n_{rot} \geq$ 1200 rpm due to the negligible liquid flow relative to the packing material in the circumferential direction. These results suggest that a ZZ packing without support rods

(manufactured as a single segment) might not show any variation in the liquid fraction in the circumferential direction at any n_{rot}. Note, this hypothesis was not proven in this study.

The average liquid fractions in the packing $\bar{\varepsilon}_L$ for the upper and lower baffle layers at fluid flow rates $\dot{V}_{G,3}$ = 1 m^3 h^{-1}, $\dot{V}_{L,3}$ = 0.96 m^3 h^{-1} and $\dot{V}_{G,1}$ = 0.5 m^3 h^{-1}, $\dot{V}_{L,1}$ = 0.48 m^3 h^{-1} are given in Figure 10.

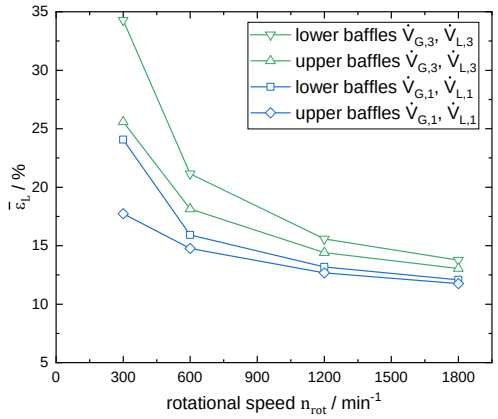

Figure 10. Effect of rotational speed n_{rot} on the average liquid fractions $\bar{\varepsilon}_L$ in the unstacked ZZ packing at fluid flow rates of $\dot{V}_{G,1}$ = 0.5 m^3 h^{-1} air , $\dot{V}_{L,1}$ = 0.48 m^3 h^{-1} tap water (blue) at the upper (upward pointing triangle) and lower (downward pointing triangle) baffle layers of the unstacked ZZ packing and at fluid flow rates of $\dot{V}_{G,3}$ = 1 m^3 h^{-1} air, $\dot{V}_{L,3}$ = 0.96 m^3 h^{-1} tap water (green) at the upper (diamonds) and lower (squares) baffle layers of the ZZ packing at 300 to 1800 rpm at 20°C and atmospheric pressure. The data are given in Table S4 in the Supporting Information.

With increasing n_{rot}, $\bar{\varepsilon}_L$ asymptotically approaches a minimum value. This can be explained by a minimum amount of liquid being retained on the baffles even at high n_{rot}. $\bar{\varepsilon}_L$ at 1800 rpm decreases with decreasing fluid flow rates due to the lower liquid loads between the baffles. $\bar{\varepsilon}_L$ is expected to approach the theoretical minimum (with liquid only in the cavity of the baffles) of

6.1 % in the upper half of the packing (14 baffles) and 6.5 % in the lower half of the packing (15 baffles) for liquid flow rates close to zero, at sufficiently high n_{rot}.

The increasing absolute values and slope of $\bar{\varepsilon}_L$ over n_{rot} with increasing fluid load confirm the argument of an increased liquid holdup in the rotor causing the increasing frictional pressure drop with decreasing n_{rot} and ultimately the formation of a pressure drop minimum (see section 3.1).

Conclusion

In this study, the fluid dynamics and in particular the liquid holdup in 3D-printed ZZ packings were investigated using total wet pressure drop, a sight glass on top of the rotor eye and gamma-ray computed tomography. In addition, the fluid dynamics in single-level ZZ packing and newly introduced stacked two-level ZZ packing were compared.

For rotational speeds < 500 rpm, a pulsating liquid wreath formed in the rotor eye in front of the unstacked ZZ packing, which was indicated by a sharp increase in pressure drop. Lower than 300 rpm, large amounts of water accumulated in the rotor eye, from which gas bubbles erupted. The stacked two-level ZZ packing showed the same fluid-dynamic behavior compared to the single-level ZZ packing. Further, the gamma-ray computed tomography allowed a clear identification of the individual baffles of the ZZ packing and of the liquid holdup on each baffle. It was shown that the ZZ structure provides a uniform liquid distribution in radial, circumferential and axial directions throughout the entire packing volume at $n_{rot} \geq 1200$ rpm.

As shown in this study, gamma-ray computed tomography proved to be an excellent tool to determine the liquid distribution inside a packing. Therefore, for the development of new types of packing with novel structures, gamma-ray computed tomography should generally be considered to study the liquid distribution.

AUTHOR INFORMATION

Author Contributions

All authors contributed to the preparation of the manuscript. All authors approved the final version of the manuscript.

Notes

The authors declare no competing financial interests.

ABBREVIATIONS

Symbols

A_c = Cross-sectional area, m^2

F_G = Gas capacity factor, $Pa^{0.5}$

H = Height of packing, m

h = Height of baffles, m

K_{O_2,H_2O}^{px} = Henry's volatility coefficient, mol bar mol^{-1}

LL = Liquid load, $m^3\ m^{-2}\ h^{-1}$

n_{rot} = Rotational speed, rpm

n_{th} = number of theoretical stages, -

$\dot{n}$ = Molar flow rate, mol h^{-1}

p = Pressure, Pa

R_i = Radius of the inner packing edge, m

$r_{i,baffle\ j}$ = Inner radius of baffle j, m

R_o = Radius of the outer packing edge, m

$r_{o,baffle\ j}$ = Outer radius of baffle j, m

$\dot{V}$ = Volumetric flow rate, $m^3\ h^{-1}$

w_{baffle} = Baffle width, mm

w_w = Weir width, mm

x = Mole fraction in the liquid phase, mol mol^{-1}

y = Mole fraction in the gas phase, mol mol^{-1}

Δh = Axial overlap of baffles, mm

Greek symbols

$\varepsilon_L(i,k)$ = Liquid fraction at pixel position i and k, %

$\varepsilon_{L,aa}(r)$ = Angular-averaged liquid fraction at radius r, %

$\bar{\varepsilon}_L$ = Average liquid fraction in the packing, %

$\mu_{\mathrm{dry}}(i,k)$ = Reconstructed attenuation coefficients distribution in dry RPB at pixel position i and k, -

$\bar{\mu}_{\mathrm{liq}}$ = Attenuation reference value of liquid phase, -

$\mu_{\mathrm{op}}(i,k)$ = Reconstructed attenuation coefficients distribution during RPB operation at pixel position i and k, -

ρ = Density, kg m^{-3}

Subscripts and superscripts

G = Gas

H2O = Water

in = Inlet

L = Liquid

O2 = Oxygen

out = Outlet

ZP = Zickzack packing

Abbreviations

CT = Computed tomography

HiGee = High gravity

RPB = Rotating packed bed

ZZ packing = Zickzack packing

Supporting Information

Total wet pressure drop data in the RPB equipped with an unstacked ZZ packing; Total wet pressure drop data in the RPB equipped with a single-level ZZ packing and a two-level ZZ packing; Number of theoretical stages data in the RPB equipped with a single-level ZZ packing and two-level ZZ packing; Liquid fraction distribution in the upper and lower layer of baffles of the unstacked ZZ packing at $\dot{V}_{G,3}$ and $\dot{V}_{L,3}$; Liquid distribution and corresponding Zickzack structure in the unstacked Zickzack packing; Angular-averaged radial profiles of the liquid fraction and the liquid fraction distribution in an unstacked ZZ packing with 454 mm outer diameter at $\dot{V}_{G,3}$ and $\dot{V}_{L,3}$; Angular-averaged radial profiles of the liquid fraction and liquid fraction distributions in the studied unstacked ZZ packing at $\dot{V}_{G,1}$ and $\dot{V}_{L,1}$; Liquid fraction distribution in the upper and lower layer of baffles of the unstacked ZZ packing at $\dot{V}_{G,1}$ and $\dot{V}_{L,1}$; Average liquid fractions data in the unstacked ZZ packing.

The Supporting Information is available free of charge from the ACS Publications website.

References

(1) Ramshaw, C.; Mallinson, R. H. Mass transfer process **1981** (US Patent No. 4283255).

(2) Cortes Garcia, G. E.; van der Schaaf, J.; Kiss, A. A. A Review on Process Intensification in HiGee Distillation. *J. Chem. Technol. Biotechnol.* **2017**, *92* (6), 1136–1156. DOI: 10.1002/jctb.5206.

(3) Neumann, K.; Gladyszewski, K.; Groß, K.; Qammar, H.; Wenzel, D.; Górak, A.; Skiborowski, M. A Guide on the Industrial Application of Rotating Packed Beds. *Chem. Eng. Res. Des.* **2018**, *134*, 443–462. DOI: 10.1016/j.cherd.2018.04.024.

(4) Guo, J.; Jiao, W.; Qi, G.; Yuan, Z.; Liu, Y. Applications of High-Gravity Technologies in Gas Purifications: A Review. *Chin. J. Chem. Eng.* **2019**, *27* (6), 1361–1373. DOI: 10.1016/j.cjche.2019.01.011.

(5) Rao, D. P.; Bhowal, A.; Goswami, P. S. Process Intensification in Rotating Packed Beds (HIGEE): An Appraisal. *Ind. Eng. Chem. Res.* **2004**, *43* (4), 1150–1162. DOI: 10.1021/ie030630k.
(6) Hendry, J. R.; Lee, J. G.M.; Attidekou, P. S. Pressure drop and flooding in rotating packed beds. *Chem. Eng. Process.* **2020**, *151*, 107908. DOI: 10.1016/j.cep.2020.107908.
(7) Agarwal, L.; Pavani, V.; Rao, D. P.; Kaistha, N. Process Intensification in HiGee Absorption and Distillation: Design Procedure and Applications. *Ind. Eng. Chem. Res.* **2010**, *49* (20), 10046–10058. DOI: 10.1021/ie101195k.
(8) Fowler, R.; Gerdes, K. F.; Nygaard, H. F. A Commercial-Scale Demonstration of Higee for Bulk CO_2 Removal and Gas Dehydration. Paper presented at the Offshore Technology Conference, Houston, Texas, May **1989**, Paper Number: OTC-6121-MS. DOI: 10.4043/6121-MS.
(9) Zhao, H.; Shao, L.; Chen, J.-F. High-Gravity Process Intensification Technology and Application. *Chem. Eng. J.* **2010**, *156* (3), 588–593. DOI: 10.1016/j.cej.2009.04.053.
(10) Groß, K.; de Beer, M.; Dohrn, S.; Skiborowski, M. Scale-Up of the Radial Packing Length in Rotating Packed Beds for Deaeration Processes. *Ind. Eng. Chem. Res.* **2020**, *59* (23), 11042–11053. DOI: 10.1021/acs.iecr.0c00868.
(11) Groß, K.; Bieberle, A.; Gladyszewski, K.; Schubert, M.; Hampel, U.; Skiborowski, M.; Górak, A. Analysis of Flow Patterns in High-Gravity Equipment Using Gamma-Ray Computed Tomography. *Chem. Ing. Tech.* **2019**, *91* (7), 1032–1040. DOI: 10.1002/cite.201800085.
(12) Zhao, B.; Tao, W.; Zhong, M.; Su, Y.; Cui, G. Process, Performance and Modeling of CO_2 Capture by Chemical Absorption using High Gravity: A Review. *Renew. Sustain. Energy Rev.* **2016**, *65*, 44–56. DOI: 10.1016/j.rser.2016.06.059.
(13) Loll, R.; Koop, J. 7 3D printed packings for rotating packed beds. In *Process Intensification*; Skiborowski, M., Górak, A., Eds.; De Gruyter, 2022; pp 189–208. DOI: 10.1515/9783110724998-007.
(14) Wen, Z.-N.; Wu, W.; Luo, Y.; Zhang, L.-L.; Sun, B.-C.; Chu, G.-W. Novel Wire Mesh Packing with Controllable Cross-Sectional Area in a Rotating Packed Bed: Mass Transfer Studies. *Ind. Eng. Chem. Res.* **2020**, *59* (36), 16043–16051. DOI: 10.1021/acs.iecr.0c01886.
(15) Wu, W.; Luo, Y.; Chu, G.-W.; Su, M.-J.; Cai, Y.; Zou, H.-K.; Chen, J.-F. Liquid Flow Behavior in a Multiliquid-Inlet Rotating Packed Bed Reactor with Three-Dimensional Printed Packing. *Chem. Eng. J.* **2020**, *386*, 121537. DOI: 10.1016/j.cej.2019.04.117.
(16) Qammar, H.; Gładyszewski, K.; Górak, A.; Skiborowski, M. Towards the Development of Advanced Packing Design for Distillation in Rotating Packed Beds. *Chem. Ing. Tech.* **2019**, *91* (11), 1663–1673. DOI: 10.1002/cite.201900053.
(17) Lukin, I.; Wingartz, I.; Schembecker, G. Application of Rotating Packed Bed for In-Line Aroma Stripping from Cell Slurry. *J. Chem. Technol. Biotechnol.* **2020**, *95* (11), 2834–2841. DOI: 10.1002/jctb.6493.
(18) Loll, R.; Runge, L.; Koop, J.; Held, C.; Schembecker, G. Zickzack Packings for Deaeration in Rotating Packed Beds─Improved Rotor Design to Counter Bypass Flows. *Ind. Eng. Chem. Res.* **2022**, *61* (32), 11934–11946. DOI: 10.1021/acs.iecr.2c01443.
(19) Zhang, W.; Xie, P.; Li, Y.; Teng, L.; Zhu, J. Hydrodynamic characteristics and mass transfer performance of rotating packed bed for CO2 removal by chemical absorption: A review. *J. Nat. Gas Eng.* **2020**, *79*, 103373. DOI: 10.1016/j.jngse.2020.103373.

(20) Ghadyanlou, F.; Azari, A.; Vatani, A. A Review of Modeling Rotating Packed Beds and Improving Their Parameters: Gas–Liquid Contact. *Sustainability* **2021**, *13* (14), 8046. DOI: 10.3390/su13148046.
(21) Burns, J. R.; Ramshaw, C. Process intensification: Visual study of liquid maldistribution in rotating packed beds. *Chem. Eng. Sci.* **1996**, *51* (8), 1347–1352. DOI: 10.1016/0009-2509(95)00367-3.
(22) Bašić, A.; Duduković, M. P. Liquid holdup in rotating packed beds: Examination of the film flow assumption. *AIChE J.* **1995**, *41* (2), 301–316. DOI: 10.1002/aic.690410212.
(23) Burns, J. R.; Jamil, J. N.; Ramshaw, C. Process Intensification: Operating Characteristics of Rotating Packed Beds — Determination of Liquid Hold-Up for a High-Voidage Structured Packing. *Chem. Eng. Sci.* **2000**, *55* (13), 2401–2415. DOI: 10.1016/S0009-2509(99)00520-5.
(24) Yang, Y.; Xiang, Y.; Chu, G.; Zou, H.; Luo, Y.; Arowo, M.; Chen, J.-F. A noninvasive X-ray technique for determination of liquid holdup in a rotating packed bed. *Chem. Eng. Sci.* **2015**, *138*, 244–255. DOI: 10.1016/j.ces.2015.07.044.
(25) Liu, Y.-Z.; Luo, Y.; Chu, G.-W.; Liu, W.; Shao, L.; Chen, J.-F. Liquid holdup and wetting efficiency in a rotating trickle-bed reactor. *AIChE J.* **2019**, *65* (8). DOI: 10.1002/aic.16618.
(26) Gładyszewski, K.; Groβ, K.; Bieberle, A.; Schubert, M.; Hild, M.; Górak, A.; Skiborowski, M. Evaluation of Performance Improvements through Application of Anisotropic Foam Packings in Rotating Packed Beds. *Chem. Eng. Sci.* **2021**, *230*, 116176. DOI: 10.1016/j.ces.2020.116176.
(27) Groß, K. M. Deaeration in Rotating Packed Beds. Ph. D. Dissertation, TU Dortmund University, Dortmund, DE, **2021**.
(28) Hampel, U.; Bieberle, A.; Hoppe, D.; Kronenberg, J.; Schleicher, E.; Sühnel, T.; Zimmermann, F.; Zippe, C. High resolution gamma ray tomography scanner for flow measurement and non-destructive testing applications. *Rev. Sci. Instrum.* **2007**, *78* (10), 103704. DOI: 10.1063/1.2795648.
(29) Kak, A.; Slaney, M. Principles of Computerized Tomographic Imaging. *IEEE Press* **1988**.
(30) Bieberle, A.; Neumann, M.; Hampel, U. Advanced process-synchronized computed tomography for the investigation of periodic processes. *Rev. Sci. Instrum.* **2018**, *89* (7), 73111. DOI: 10.1063/1.5038423.
(31) Li, Y.; Lu, Y.; Wang, G.; Nie, Y.; Ying, H.; Ji, J.; Liu, X. Liquid Entrainment and Flooding in a Rotating Zigzag Bed. *Ind. Eng. Chem. Res.* **2015**, *54* (9), 2554–2563. DOI: 10.1021/ie5019904.
(32) Neumann, K.; Hunold, S.; Skiborowski, M.; Górak, A. Dry Pressure Drop in Rotating Packed Beds—Systematic Experimental Studies. *Ind. Eng. Chem. Res.* **2017**, *56* (43), 12395–12405. DOI: 10.1021/acs.iecr.7b03203.
(33) van Aarle, W.; Palenstijn, W. J.; Beenhouwer, J. de; Altantzis, T.; Bals, S.; Batenburg, K. J.; Sijbers, J. The ASTRA Toolbox: A platform for advanced algorithm development in electron tomography. *Ultramicroscopy* **2015**, *157*, 35–47. DOI: 10.1016/j.ultramic.2015.05.002. Published Online: May. 6, 2015.